Machine Learning approaches for the design of biomechanically compatible bone tissue engineering scaffolds

Silvia Ibrahimi [a], Luca D'Andrea [b], Dario Gastaldi [b], Massimo W. Rivolta [a], Pasquale Vena [b],*

[a] *Dipartimento di Informatica, Università degli Studi di Milano, Milan, Italy*
[b] *Department of Chemistry, Materials and Chemical Engineering "Giulio Natta", Laboratory of Biological Structure Mechanics (LaBS) - Politecnico di Milano, Piazza Leonardo da Vinci 32, 20133, Milano, Italy*

A R T I C L E I N F O

A B S T R A C T

Triply-Periodic Minimal Surfaces (TPMS) analytical formulation does not provide a direct correlation between the input parameters (analytical) and the mechanical and morphological properties of the structure. In this work, we created a dataset with more than one thousand TPMS scaffolds for the training of Machine Learning (ML) models able to find such correlation. Finite Element Modeling and image analysis have been used to characterize the scaffolds. In particular, we trained three different ML models, exploring both a linear and non-linear approach, to select the features able to predict the input parameters. Furthermore, the features used for the prediction can be selected in three different modes: i) fully automatic, through a greedy algorithm, ii) arbitrarily, by the user and iii) in a combination of the two above methods: i.e. partially automatic and partially through a user-selection. The latter, coupled with the non-linear ML model, exhibits a median error less than 3% and a determination coefficient higher than 0.89 for each of the selected features, and all of them are accessible during the design phase. This approach has been applied to the design of a hydroxyapatite TPMS scaffolds with prescribed properties obtained from a real trabecular-like hydroxyapatite scaffold. The obtained results demonstrate that the ML model can effectively design a TPMS scaffold with prescribed features on the basis of biomechanical, mechanobiology and technological constraints.

1. Introduction

Trauma, diseases and surgical interventions may cause critical-size bone defects which cannot heal spontaneously through the self-repair process of the bone [1]. Conventional therapy usually involves the use of autograft and allograft; which, however, have important limitations [2]. Considering that bone is the second most transplanted biological tissue in the world and that the incidence of the problem is becoming more prevalent in the population, it is imperative to find alternative solutions [3]. Synthetic bone substitutes, also known as scaffolds, appear to be a promising solution [4,5]. Bone Tissue Engineering (BTE) is a multidisciplinary field that combines principles from various disciplines to develop innovative approaches for repairing and regenerating bone tissue. It involves the application of engineering, biology, materials science, and medicine to design and create functional artificial bone constructs that can replace or stimulate the regeneration of damaged or lost bone [6].

Additive Manufacturing (AM) techniques have been proved to be able to produce scaffolds with complex microstructures with high accuracy, offering high flexibility in the architectural design of the scaffolds allowing to meet the multi-disciplinary

---

requirements for the optimal design of the scaffolds, simultaneously [7]. The design of an effective scaffold is a non-trivial process that is still far from being consolidated. Load-bearing applications of BTE scaffolds impose particular emphasis on the mechanical properties [8,9] which may be in contrast with the concurrent need for high porosity and pore interconnectivity.

It is well-known that the scaffold's geometrical features have an impact on its osteo-integration response. In particular, pore size/porosity as well as pore shapes have a direct impact on macroscopic scaffold permeability which is responsible for nutrient transport [10]. The superficial strain on the internal walls of the pores may also play a relevant role in determining the mineralization process [11]. Indeed, as bio-mechanical, physical and biological factors are involved, a large number of design variables are needed; this implies time-consuming experimental protocols for the in-vitro characterization of the effect of each single design parameter [12].

The mechanical properties of bio-inspired cellular structures were first investigated in the 80's [13,14]. These fundamental studies based on analytical predictions nourished many recent approaches, based on computational methods, aimed at designing optimal microstructures for BTE scaffolds. New scaffold architectures based on Triply-Periodic Minimal Surfaces (TPMS) topology, such as Gyroid (G), Schwartz Diamond (D) or Schoen's Wrapped Package (IWP), have been investigated [15–17]. In contrast to stochastic structures, regular porous architectures have more homogeneous stress distribution allowing for a better control of the mechanical properties and hence on the long-term performance of the devices [17]. Topology optimization is a powerful tool to achieve optimal design meeting multi-objective design criteria [18,19]; however, computational costs increase substantially with the design variables and iterations. Machine Learning (ML) techniques offer optimization algorithms that are particularly effective when dealing with large datasets providing empirical models also in absence of physics-based models [20].

The application of Artificial Intelligence (AI) in biomaterials design has been growing in recent years, likely due to the proven effectiveness of this type of techniques in processing large amount of data, often heterogeneous by nature, achieved in other fields (e.g., Computer Vision). The scaffold design process indeed involves generation of data at different levels of the pipeline. For example, the design of the geometrical model of the scaffold usually requires a dataset of images collected through computed tomography or magnetic resonance, then complex algorithms are executed for segmenting the tissue [21], reconstructing the volume [22], and finally producing the blueprint for 3D printing [23].

In several studies, AI has been employed as a tool for predicting the mechanical and morphometric characteristics of scaffolds (see for instance [24,25]). However, the application of AI techniques to estimate the geometric characteristics of scaffolds based on specific physical properties is relatively less explored, with a limited number of projects focusing on this area [26–28].

The aim of this paper is to set up a multidisciplinary optimization tool for the identification of the design of a scaffold based on TPMS topologies exhibiting prescribed mechanical, physical or morphometric target properties. To this purpose, a complete pipeline for designing ML algorithms is implemented. Using such pipeline, two models with different complexity have been investigated. In particular, the first model relies on a linear relationship between properties and TPMS design parameters, whereas the second incorporates a non-linear function. The performance of linear and non-linear models are compared to select the optimal one. Then, a variant of the non-linear model with optimization constraints has been tested as well. The ML models are trained by using a dataset created by multiple running of the forward problem which, starting from prescribed values of the design variables, estimates the mechanical, physical and micro-architectural properties by means of the finite element (FE) method and image process analyses. The performance of the obtained optimization tool is then tested by prescribing design requirements in terms of preselected mechanical, physical and microarchitectural features comparing the performance of the predicted optimal scaffold architectures with the prescribed design requirements.

2. Materials and methods

2.1. Summary of the overall pipeline

The proposed methodology is intended to support the identification of optimal TPMS architectures by leveraging biomechanical and morphometric parameters as design requirements. Since a physics-based model linking such parameters and TPMS designs is currently not available, we rely on the use of supervised ML to create a functional relationship.

The approach employed is to generate a set of scaffolds through the free parameters of the mathematical formulation of TPMS architectures. The generated scaffolds have been represented by three-dimensional image stacks. Once the three-dimensional scaffolds have been created, FE simulations and image analyses have been executed to solve the forward problem and to provide a list of features for each of the scaffold. Such list contains mechanical, physical and morphometric characteristics. This approach generates a dataset with TPMS input parameters paired with the quantified features. Then, a subset of these features has been either manually or automatically selected as design requirements for the scaffold. Three feature selection schemes will be proposed. A ML model has been finally created to predict the optimal TPMS parameters by means of the selected features.

The structure of this section is as follows: the computational tools used to build the above-mentioned dataset (solution of the forward problem) are introduced with subsections for the definition of the scaffold architecture, the morphometric features, the effective pore connectivity and the mechanical analysis; a section will describe the ML algorithm; the last section will describe the procedure for the assessment of the performances of the optimization algorithm.
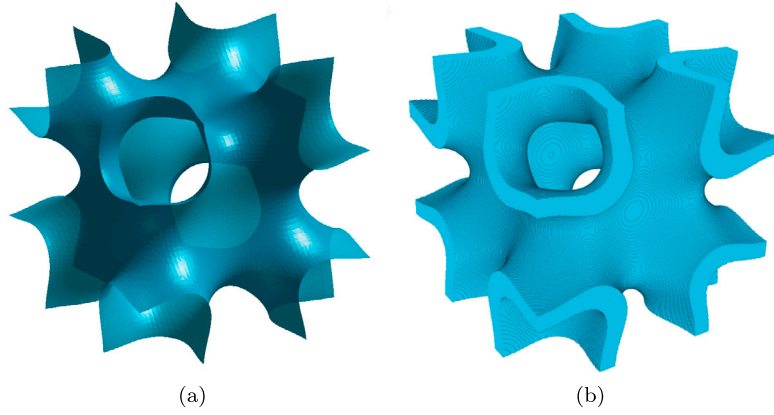
(a)   (b)

Fig. 1. Example of a repetitive unit of IWP geometry with its (a) surface obtained using (1) and (b) volume obtained with (2).

2.2. Scaffold design

The scaffolds analyzed in the study are characterized by TPMS geometries. The most common approach to the geometric description of TPMS surfaces is through the definition of implicit trigonometric functions which defines a sheet network. In this work, three architectures have been considered: (i) Diamond, (ii) Gyroid and (iii) IWP, which have been defined through the following implicit functions $f(x, y, z)$.

The mathematical three-dimensional surface $f(x, y, z) = 0$ defining the TPMS are:

$$f_D = \cos(kx)\cos(ky)\cos(kz) - \sin(kx)\sin(ky)\sin(kz) + b$$
$$f_G = \sin(kx)\cos(ky) + \sin(ky)\cos(kz) + \sin(kz)\cos(kz) + b \tag{1}$$
$$f_I = 2[\cos(kx)\cos(ky) + \cos(ky)\cos(kz) + \cos(kz)\cos(kx)] - \cos(2kx) - \cos(2ky) - \cos(2kz) + b$$

in which the subscripts D, G and I refer to the Diamond, Gyroid and IWP geometry, respectively. When generating scaffolds, a discrete formulation is employed: $k = 2\pi c/n$. Given a cubic cell, c represents the number of repetitive units and n the voxels per edge. In this work, $c = 3$ and $n = 300$. The spatial coordinates x, y and z are integer numbers from 1 to n. The solid volume has been generated by providing a thickness on the above-reported surfaces in a pixel-wise fashion. The pixels belonging to the solid part are those fulfilling the conditions:

$$-\delta < f(x, y, z) < \delta \tag{2}$$

We consider b and δ as the free TPMS input parameters used to generate the geometries. Fig. 1 shows an example of the mid surface generated through the implicit trigonometric functions and the corresponding solid scaffold.

The scaffolds have been automatically generated as a stack of binary images through a MATLAB script by setting the parameters b and δ. The values of b range from 0 to 2 with a step of 0.1, whereas the values of δ range from 0.4 to 1.5 with a step of 0.05, as similarly done by [29]. The scaffolds exhibiting entirely empty slices, fully solid slices or pinching off of the surface [30] have been discarded. In addition, we only considered connected structures on which a connectivity analysis has been carried out. The scaffolds fulfilling all the previously defined conditions resulted in 1279 designs (321, 475, and 483 designs for Diamond, Gyroid and IWP, respectively).

2.3. Morphometric analysis

The following morphometric parameters have been calculated from the generated TPMS scaffolds: volumetric fraction (ρ^*), Trabecular Thickness (Tb.Th.), Trabecular Spacing (Tb.Sp.), Connectivity (Conn.), Ellipsoid Factor (EF), and the Degree of Anisotropy (DA). These parameters have been computed by means of the BoneJ plugin of the open-source software ImageJ [31]. Despite the software has been designed to process bone structures, it offers the functionality to extract such features from any geometry, hence we used it on our TPMS models. The Tb.Th. and Tb.Sp. parameters have to be intended as wall thickness and pore spacing, respectively. A Java language macro has been developed with the purpose of sequentially calculating the morphometric parameters for all scaffolds belonging to the dataset. These analyses have been performed on a Linux machine equipped with 8 $CPUs$ with a RAM of 86 GB.

2.4. Permeability analysis

In this study, the hydraulic permeability has been represented by a simplified permeability index: the Effective Pore Connectivity Index (EPCI). Such index has been obtained by processing the 3D images of each scaffold, and used to estimate permeability in

accordance with the methodology suggested by Sun et al. [32]. Under the assumption of fully saturated porous material, the EPCI index is calculated by tracking the connectivity of pores within a scaffold. To this purpose, a MATLAB code has been created to sequentially calculate the EPCI on all scaffolds belonging to the dataset.

2.5. Mechanical properties

The macroscopic mechanical parameters have been computed through FE simulations performed on each scaffold. All FE analyses have been carried out on a voxel-type mesh (defined on the three-dimensional matrix described in Section 2.2), where each voxel corresponds to a linear hexahedron with three-linear shape functions. The multi-grid parallel finite element solver ParOSol has been used [33]. As microstructured solids exhibiting TPMS micro-architecture are characterized by a macroscopic elastic tensor with cubic symmetry (three independent parameters) [29], only two FE simulations have been carried out to fully characterize the elastic properties: a uniaxial confined tension with prescribed displacement on one face of the cubic macroscopic domain and a pure macroscopic shear. The boundary conditions used in the two types of simulations are reported below:

$$\begin{cases} u_x|_{\partial V} = x\bar{\varepsilon} \\ u_y|_{\partial V} = 0 \\ u_z|_{\partial V} = 0 \end{cases} \quad ; \quad \begin{cases} u_x|_{\partial V} = y\bar{\gamma} \\ u_y|_{\partial V} = 0 \\ u_z|_{\partial V} = 0 \end{cases} \tag{3}$$

where u_x, u_y, and u_z are the cartesian components of the displacement vector, $\bar{\varepsilon}$ the macroscopic direct strain, $\bar{\gamma}$ the macroscopic shear strain, and ∂V the external boundary of the cubic volume V defined by the scaffold. The six components of the Cauchy stress tensor have been averaged on the cubic macroscopic domain of the scaffold to obtain the components C_{ij} of the homogenized stiffness tensor $\mathbf{C}$. The normalized macroscopic stiffness ($\bar{E}/E_0$), the normalized macroscopic shear stiffness ($\bar{G}/E_0$) and the macroscopic Poisson coefficient ($\bar{v}$) have been computed as follows:

$$\frac{\bar{E}}{E_0} = \frac{C_{11}^2 + C_{11}C_{21} - 2C_{21}^2}{C_{21} + C_{11}}; \qquad \frac{\bar{G}}{E_0} = C_{44}; \qquad \bar{v} = \frac{C_{21}}{C_{21} + C_{11}} \tag{4}$$

where C_{11} and C_{21} have been obtained from the uniaxial confined tension, whereas C_{44} from the pure macroscopic shear. Furthermore, the Zener ratio (α_Z) has been calculated as an indicator of mechanical anisotropy [34,35].

Normalized macroscopic elastic moduli and shear stiffness have been obtained by using a reference value of the elastic modulus (1 GPa) and a Poisson coefficient of 0.3 as intrinsic properties of the solid material. The elastic modulus and shear stiffness of scaffolds can be obtained by multiplying the output of the simulation ($\bar{E}/E_0$ and $\bar{G}/E_0$), which comes in a normalized form, by the elastic modulus of the constituent material. In this study, hydroxyapatite has been used as a material of choice for the BTE scaffolds therefore, an elastic modulus of the material (E_0) has been set to 100 GPa [36], to obtain the macroscopic Young modulus ($\bar{E}$) and the macroscopic shear stiffness ($\bar{G}$).

The approach based on the Weibull probability model, proposed by Genet et al. [37] has been adopted to obtain the index of strength (I_σ) under uniaxial compression. I_σ is associated with a 95% probability of failure and has been calculated for each design as follows:

$$I_\sigma = \left(\frac{ln\left(\frac{1}{1-P^F}\right)}{\frac{1}{V_{eff}} \int_V \|\langle\varepsilon\rangle_+\|^m \, dV} \right)^{\frac{1}{m}} \cdot \bar{E}\bar{\varepsilon} \tag{5}$$

where P^F is the probability of failure, V defines the solid volume of the scaffold, V_{eff} is the reference volume equal to 1 mm^3 [37], m is the Weibull modulus (equal to 6.6 [38]); $\langle\varepsilon\rangle_+$ denotes the positive part of the maximum principal strain. FE analyses have been run on the same machine reported in Section 2.3.

2.6. Machine learning algorithms

2.6.1. The dataset

The quantities determined in the forward problem have been rearranged to form a dataset suitable for the ML problem. In particular, for each ith geometry generated, 37 features have been stored in the column vector $\mathbf{x}_i$ along with the associated b_i, δ_i and geometry type t_i. Formally, a dataset has been constructed as the set $\mathcal{X} = \{(\mathbf{x}_i, b_i, \delta_i, t_i)\}_{i=1}^N$ where N is the total number of scaffolds, equal to 1226. This number is lower than the total number of analyzed scaffolds (1279) since for some of them it was not possible to compute the entire set of 37 features (for IWP scaffolds exhibiting a wall thickness equal or below 4 pixels). A brief description of the main important features has been reported in Sections 2.3–2.5, whereas the list of all extracted features, along with their detailed description, is reported in Table 3 of Supplementary Material.

The dataset has been randomly partitioned into a training set (60%), validation set (20%) and test set (20%). Training set and validation set have been used for selecting the most important features, while the test set has been used to compare the performance of the models (Table 1). In addition, a subset of 50 random samples has been extracted from the test set for further assessment (see Section 2.7).

Table 1
Dataset split among training set, validation set and test set. Within each set, the columns display the number and percentage of scaffolds corresponding to different geometries.

Geometry	Training set		Validation set		Test set	
Diamond	203	27.6%	57	23.3%	61	24.9%
Gyroid	285	38.7%	104	42.4%	86	35.1%
IWP	248	33.7%	84	34.3%	98	40.0%
	736	100%	245	100%	245	100%

2.6.2. The ML model

ML was used to solve the inverse problem, that is, to determine the design parameters b, δ and type of geometry t from some of the scaffold features obtained in the forward problem. The selection of a ML model appropriate for the application to tackle is an open problem. The model is typically chosen, within a pool of models, as the one with the lowest empirical prediction error. In this study, we developed and compared three models: one linear model which has served as a baseline for performance comparisons, and two non-linear models.

Each model comprises three components. The first two components were specifically constructed to predict the b and δ values based on a certain set of features. The third component was built to predict the geometry type t (i.e. Gyroid, Diamond and IWP), based on the same set of features.

The components of all models could be described as follows:

$$\hat{b}_i = f_{\mathbf{w}_b}(\mathbf{x}_i)$$
$$\hat{\delta}_i = g_{\mathbf{w}_\delta}(\mathbf{x}_i)$$
$$\Pr(T_i = t|\mathbf{x}_i) = \text{softmax}([h_{\mathbf{w}_G}(\mathbf{x}_i), h_{\mathbf{w}_D}(\mathbf{x}_i), h_{\mathbf{w}_I}(\mathbf{x}_i)]^\intercal)_t, \qquad \hat{t}_i = \arg\max_t \Pr(T_i = t|\mathbf{x}_i) \tag{6}$$

where $\mathbf{x}_i$ is a column vector containing the features of the ith sample with dimension P, $\mathbf{w}_b$, $\mathbf{w}_\delta$, $\mathbf{w}_G$, $\mathbf{w}_D$ and $\mathbf{w}_I$ are column vectors storing the model parameters, $\hat{b}_i$ and $\hat{\delta}_i$ represent the predicted values and $\Pr(T_i = t|\mathbf{x}_i)$ is the conditional probability of classifying the geometry type as t conditioned on the feature vector $\mathbf{x}_i$. The number of P can vary between 1 and 37, according to the index J defined in Section 2.6.3 and evaluated in Section 3.2. The final prediction for the geometry $\hat{t}_i$ has been obtained by that one maximizing the probability $\Pr(T_i = t|\mathbf{x}_i)$ across $t \in \{G, D, I\}$. The softmax function converts a vector of numbers into another normalized vector whose elements sum to 1. The value $\text{softmax}(\cdot)_t$ is the tth component of such normalized vector. The approach for predicting the geometry type is equivalent to a multinomial logistic regression model. To conclude, the parametric functions $f_{\mathbf{w}_b}$, $g_{\mathbf{w}_\delta}$, $h_{\mathbf{w}_G}$, $h_{\mathbf{w}_D}$ and $h_{\mathbf{w}_I}$ describe the full model. Each of the three models has its own components and parameter vectors.

The baseline linear model has been defined as follows:

$$f_{\mathbf{w}_b}(\mathbf{x}_i) = \mathbf{w}_b^\intercal \mathbf{x}_i$$
$$g_{\mathbf{w}_\delta}(\mathbf{x}_i) = \mathbf{w}_\delta^\intercal \mathbf{x}_i$$
$$h_{\mathbf{w}_G}(\mathbf{x}_i) = \mathbf{w}_G^\intercal \mathbf{x}_i$$
$$h_{\mathbf{w}_D}(\mathbf{x}_i) = \mathbf{w}_D^\intercal \mathbf{x}_i \tag{7}$$
$$h_{\mathbf{w}_I}(\mathbf{x}_i) = \mathbf{w}_I^\intercal \mathbf{x}_i$$

All functions embed the intercept term into the parameter vectors and by appending a 1 to $\mathbf{x}_i$. We have named this model as L-MOD.

The mathematical formulation of the non-linear model is hard to select when no information about the relationship between features and outputs are available. Considering the recent results obtained by artificial neural networks (ANN) in other domains, it may be convenient to investigate on such type of models. However, ANN are considered data-hungry models, hence requiring very large datasets. In addition, the parameter space of ANN models is typically large (even in the order of billion parameters) but, with a limited sample size, the risk of overfitting the model becomes very likely. Therefore, considering the size of the dataset at our disposal, we propose a simplification of a well-known ANN architecture, i.e. the Residual Network (ResNet), which was found very effective in many different applicative domains. The simplification is meant to adapt the ResNet to our specific problem.

The ResNet architecture comprises a sequence of blocks (composition of mathematical functions) in which each block constructs a residual output as follows:

$$\mathbf{o}_\beta = W_\beta \mathbf{o}_{\beta-1} + f_{\theta_\beta}(\mathbf{o}_{\beta-1}) \tag{8}$$

where β is the block index, W_β is a matrix of parameters and f_{θ_β} is a non-linear function parametrized by the θ_β vector. This function f_θ is typically a convolutional operator followed by a non-linear function such as hyperbolic tangent or sigmoid, suitable for processing signals and images. In this study, the model took in input, instead of raw images, the list of features. Therefore, we adapted the ResNet block to process features by removing the convolution operator. In addition, the matrix W_β and vector θ_β are usually dense and this makes the number of parameters growing rapidly. To reduce the number of parameters, we used a sparse representation of ResNet where input features are processed separately from the others using the residual approach. The final model becomes a linear combination of each feature and a non-linear function applied to it, as follows:

$$y = c + \mathbf{w}_1^\intercal \mathbf{x}_i + \mathbf{w}_2^\intercal \tanh(\text{diag}(\mathbf{w}_3)\mathbf{x}_i + \mathbf{w}_4) \tag{9}$$

where y represents b or δ depending on the parameter that is being estimated, $\mathbf{w}_1$, $\mathbf{w}_2$, $\mathbf{w}_3$, $\mathbf{w}_4$ (column vectors) and c (scalar) are the parameters of the model, $\mathrm{diag}(\mathbf{z})$ builds a diagonal matrix whose entries are the element of a generic vector $\mathbf{z}$, and $\tanh(\mathbf{z})$ is the hyperbolic tangent applied element-wise to the element of the vector $\mathbf{z}$. This model was used for predicting both b and δ, i.e. $f_{\mathbf{w}_b}$ and $g_{\mathbf{w}_\delta}$ where $\mathbf{w}_b = [\mathbf{w}_1^\intercal, \mathbf{w}_2^\intercal, \mathbf{w}_3^\intercal, \mathbf{w}_4^\intercal, c]^\intercal$ and similarly for $\mathbf{w}_\delta$. The functions h for predicting the geometry type were kept the same as for the linear case. We named this model as NL-MOD.

We designed the proposed model to have another major advantage: the additive property. Each feature has its own separate term in (9). Indeed, it is possible to write $y_i = c + \sum_k \Delta y_{i,k}$ where each $\Delta y_{i,k}$ is the contribution of only the kth feature. In particular,

$$\Delta y_{i,k} = w_{1,k} x_{i,k} + w_{2,k} \tanh(w_{3,k} x_{i,k} + w_{4,k}) \tag{10}$$

where $w_{m,k}$ and $x_{i,k}$ are the kth entry of the vector $\mathbf{w}_m$ (m from 1 to 4) and $\mathbf{x}_i$, respectively. Each term is composed by an indefinitely growing linear function of $x_{i,k}$ and a non-linear function which may saturate for extreme values of $x_{i,k}$, both weighted by the coefficients $w_{1,k}$ and $w_{2,k}$. This model is then justified in this context since many biological and physical systems are found to have this characteristic. In addition, another common property for these systems is that changing the value of a feature is often expected to affect Δy in a monotonic fashion.

The suitability of the definition in (10) for our specific application has been verified by implementing a third non-linear model which has the same mathematical formulation of (9), and adding constraints on the model parameters ensuring the monotonicity of Δy. This can be achieved by imposing the following set of constraints on the model's parameters:

$$\begin{cases} w_{3,k} = 0 \\ w_{1,k} \geq 0 \end{cases} \quad \bigcup \quad \begin{cases} w_{3,k} > 0 \\ w_{1,k} + w_{2,k}\, w_{3,k} \geq 0 \end{cases} \tag{11}$$

We named this model as NL-MOD-CON.

Using the dataset at disposal, the parameters of the three models have been obtained by minimizing the mean squared error (MSE) for both first and second models, and minimizing the MSE with constraints for the third. For the non-linear models, their parameters have been found using an iterative algorithm with initial conditions set as the coefficients found in the linear case.

2.6.3. Feature selection and model validation

Three different methods have been implemented to select relevant features that will be eventually used to predict b, δ and t parameters. The first method makes use of a fully data-driven approach by means of the so-called Greedy Feedforward Feature Selection (GFFS) algorithm [39]. Briefly, it selects features through an iterative approach. At each iteration, the optimal feature is selected from a list of candidate features. The optimal one is a single variable that is added to the set of selected variables from the previous iterations. The candidate feature obtaining the optimal performance on the validation set is selected. In addition, candidate features correlated with any of those already selected are excluded from the training. An absolute value Pearson's correlation coefficient of 0.6 was used as a threshold for the eligibility of the candidate feature. Since the objective was to find a single feature set for both b and δ, the performance metric used for selecting a feature, denoted as J, is the geometric mean between the R^2 for both outputs ($J = \sqrt{R_b^2 \cdot R_\delta^2}$), computed on the validation set. The optimal number of features has been determined by visual inspection of J across iterations. This feature set has been named Data-Driven Feature Set (DDFS).

The second feature selection scheme is based on domain knowledge. It is worth noting that not all features computed by solving the forward problem can be easily accessible in practice as a design parameter. To account for this issue, we have manually selected a list of features that we consider relevant for the problem; they are: the effective stiffness ($\bar{E}$), the index of strength (I_σ), the mean pore spacing (Tb.Sp. mean), the mean wall thickness (Tb.Th. mean) and the index of permeability (EPCI). This feature set has been named Domain Knowledge Feature Set (DKFS).

The third feature selection method is a mix of the two previous methodologies. In particular, the DDFS scheme has been used prescribing in the features selection the first three features of the DKFS scheme. This feature set has been named Mixed Feature Set (MFS).

2.7. Assessment of performance of the optimization problem

The performance of the models was quantified, on the test set, by means of (i) the R_b^2 value between the predicted $\hat{b}$ and the true values b and similarly for R_δ^2; and (ii) the accuracy of identifying the exact geometry type predicted by the multinomial logistic regression model, that is the number of correctly classified scaffolds over the total number of samples.

An additional evaluation of the performance for the proposed models has been carried out to quantify the percentage error between the design parameters ($\mathbf{x}_i$) feeding the ML models and their actual values ($\hat{\mathbf{x}}_i$) obtained after generating the scaffolds with $\hat{b}$, $\hat{\delta}$ and $\hat{t}$. In order to do so, 50 different scaffolds were randomly selected from the test set, as representative of the whole dataset. Upon the selection, the ML models predicted the optimal $\hat{b}$ and $\hat{\delta}$ and $\hat{t}$ for each selected scaffold by using their specific feature set ($\mathbf{x}_i$, input feature value in Fig. 2). Then, three-dimensional models of each scaffold have been created and the computational models described in Sections 2.3–2.5 have been used to determine the feature vectors $\hat{\mathbf{x}}_i$ (output feature values in Fig. 2). A Wilcoxon signed rank test was then used to quantify whether the percentage error between $\mathbf{x}_i$ and $\hat{\mathbf{x}}_i$ had a median value of zero (null hypothesis: median percentage error is 0, significance level set to 0.05). Fig. 2 depicts the diagram of such pipeline.
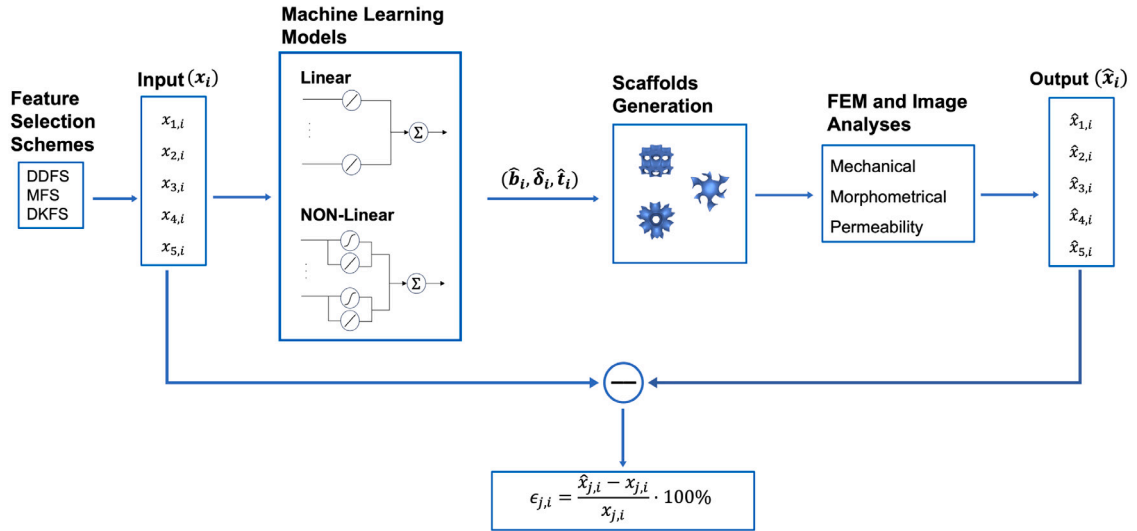
Fig. 2. Diagram for the performance evaluation of the ML models. The percentage errors $\epsilon_{j,i}$ between the input parameters $x_{j,i}$ and computed $\hat{x}_{j,i}$ were the output of the evaluation. The ith subscript refers to the geometry, whereas the jth subscript refers to the feature. A compact graphical representation of the models is depicted as well.

2.8. Design of a hydroxyapatite scaffold with given mechanical and morphological properties

The ML algorithm presented here is now applied in a use case where we find the most suitable TPMS scaffold with a given set of mechanical and morphological properties. To achieve this result, we take as a reference a trabecular-like hydroxyapatite scaffold that is fully characterized in terms of mechanical and morphological properties in [40]. The reference scaffold was obtained through a Vat Photopolymerization printing process followed by a temperature treatment for the sintering ceramic component. The 3D architecture was obtained by starting with a 3D foam model featuring a trabecular bone-like structure [41]. The aim of this application is to identify a TPMS scaffold that can be manufactured through Vat Photopolimerization and sintering of hydroxyapatite. Using a validated numerical model, D'Andrea et al. [40] determined the scaffold's macroscopic elastic modulus and compressive strength, which were found to be 7.05 GPa and 3.34 MPa, respectively. The overall porosity was 73%, while the average trabecular thickness and pore size were 318 μm ± 97 μm and 801 μm ± 224 μm, respectively. The strength index I_σ was also determined on the trabecular like hydroxyapatite scaffold and has been found $I_\sigma^{HA} = 0.89$ MPa. In particular, the following set of input parameters was used: macroscopic stiffness ($\bar{E}$), index of strength (I_σ), mean trabecular thickness (Tb.Th. mean), mean trabecular spacing (Tb.Sp. mean) and Zener coefficient (α_Z). The five input parameters for the ML algorithm, i.e. the entries of the **x** vector, are:

$$\begin{bmatrix} x_1 \\ x_2 \\ x_3 \\ x_4 \\ x_5 \end{bmatrix} = \begin{bmatrix} \bar{E}^{HA} \\ I_\sigma^{HA} \\ Tb.Sp.^{HA} \\ \alpha_Z^{HA} \\ Tb.Th.^{HA} \end{bmatrix} = \begin{bmatrix} 7.05 \text{ GPa} \\ 0.89 \text{ MPa} \\ 76 \text{ pixel} \\ 1.19 \\ 30 \text{ pixel} \end{bmatrix} \tag{12}$$

In the previous equation, the values of Tb.Sp. and Tb.Th. are reported in pixels; these correspond to 798 μm and 315 μm by considering a pixel size in the 3D image of 10.5 μm. The output of the NL-MOD with MFS has been used to identify the architecture (geometry type t and design parameters b and δ which best approximate the features and mechanical properties of the hydroxyapatite scaffold). After identification of the 5 significant features as described in Section 2.6.3, the following set of input parameters has been used: macroscopic stiffness ($\bar{E}$), index of strength (I_σ), mean trabecular thickness (Tb.Th.), mean trabecular spacing (Tb.Sp.) and Zener coefficient (α_Z).

The output of the ML algorithm has been then used to generate a pixel-like 3D image and a 3D FE mesh with cartesian voxel-like mesh. Morphometric parameters (Tb.Th. and Tb.Sp.) have been extracted from the 3D image, whereas the mechanical properties ($\bar{E}$, I_σ and α_Z) have been determined through a FE model. These parameters have been then compared with the reference values of the trabecular-like scaffold. Furthermore, the strength of the newly generated triply periodic scaffold has been also estimated by means of a FE simulation of the fracture propagation process [42] and compared with that estimated numerically in [40]. Fig. 3 shows the workflow of the process, starting from the trabecular-like scaffold used as a reference and in the end the scaffold design found through the ML algorithm.
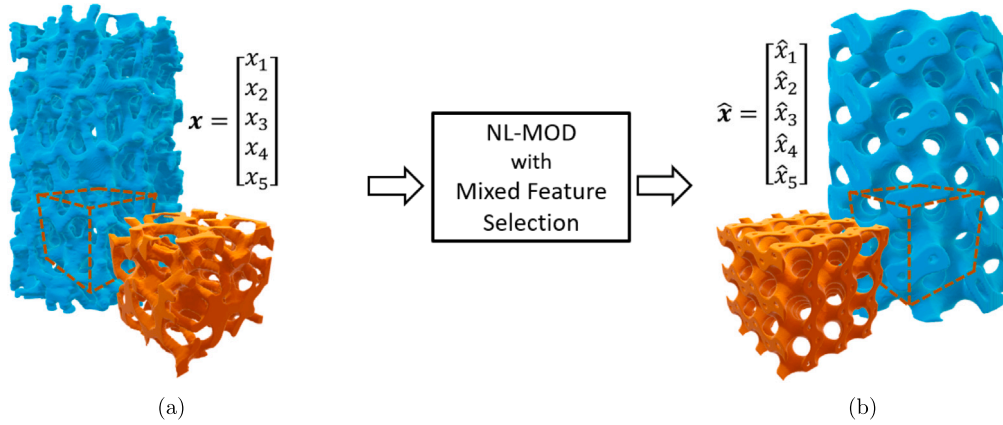
Fig. 3. (a) Trabecular-like scaffold (in blue) and its representative volume element (in orange). The vector of features **x** was extracted from the representative volume element; (b) TPMS cube (in orange) and TPMS-based scaffold (in blue). The vector of features $\hat{x}$ was extracted from the cubic domain. The meaning of the components of the vectors **x** and $\hat{x}$ is the macroscopic stiffness ($\bar{E}$), the index of strength (I_σ), the mean pore spacing (Tb.Sp. mean), the Zener (α_Z) and the mean wall thickness (Tb.Th. mean). The selection of these features has been discussed in Section 4. (For interpretation of the references to color in this figure legend, the reader is referred to the web version of this article.)

3. Results

3.1. Scaffold architectures and properties

Fig. 4 shows the domain of the design variables b and δ investigated for the Diamond, Gyroid and IWP architectures, respectively. Each dot corresponds to one specific generated scaffold. The colors of the dots represent the volumetric fraction.

For the IWP the volumetric fraction ranges from 0.1 to 0.4, while Diamond's and Gyroid's ones range from 0 to 1. As a representative example, geometrical and mechanical representations are provided for two scaffolds on the boundary of the input parameter range (Fig. 4). All three geometries show an anisotropic elastic response with cubic symmetry (i.e. $\bar{E}$, $\bar{G}$ and $\bar{\nu}$ are independent parameters). The Diamond and Gyroid architectures exhibit a higher stiffness along directions trisecting the cartesian axis in both the analyzed points. This indicates that shear stiffness in the three cartesian planes is always higher than that of an equivalent isotropic material ($\bar{G} > \frac{\bar{E}}{2(1+\bar{\nu})}$). The IWP architecture exhibits a dual trend, with the highest elastic moduli aligned along the trisecting directions ($b = 0$ and $\delta = 0.4$, Fig. 4c, left panel) and the highest elastic modulus along the cartesian directions ($b = 2$ and $\delta = 1.5$, Fig. 4c, right panel).

3.2. ML models

Fig. 5 reports the results of the selected features for the three models, determined by the GFFS algorithm using the J metric. Due to the constraint imposed in the GFFS algorithm for the maximum Pearson's correlation coefficient allowed, 16 of the 37 features are selected for L-MOD, while 17 for both NL-MOD and NL-MOD-CON. For L-MOD, J spans from 0.24 to 0.58. Regarding the non-linear models, the range of J is between 0.28 and 0.75 for NL-MOD, while 0.26 to 0.62 for NL-MOD-CON. The optimal number of selected features is 5 as the J metric did not change markedly above this number for the three models (Fig. 5). The value of J for all the combinations of features has been reported in Table 4 of Supplementary Materials.

Table 2
R^2 and accuracy for the three models and feature selection strategy computed on the test set.

Model	DDFS			MFS			DKFS		
	R_b^2	R_δ^2	Accuracy	R_b^2	R_δ^2	Accuracy	R_b^2	R_δ^2	Accuracy
L-MOD	0.78	0.35	0.92	0.81	0.36	0.90	0.70	0.32	0.92[a]
NL-MOD	0.82	0.64	0.99	0.86	0.60	0.95	0.79	0.50	0.92[a]
NL-MOD-CON	0.76	0.55	0.96	0.83	0.48	0.95	0.62	0.33	0.92[a]

[a] It is worth noting that the feature set for the DKFS group was the same across models.

Table 2 reports the R^2 values between b and $\hat{b}$ (R_b^2), and δ and $\hat{\delta}$ (R_δ^2). The R_b^2 values range from 0.62 to 0.86, while for R_δ^2, it is between 0.32 and 0.64. Also, R_b^2 exceeds R_δ^2 for all models. For both DDFS and MFS, R_b^2 and R_δ^2 are higher for the two non-linear models with respect to the linear one, while for the DKFS the L-MOD performs slightly better than the NL-MOD-CON for b.

Accuracy results are presented in Table 2. Accuracies are, in general, $\geq 90\%$. The lowest accuracy obtained is 90% with MFS of L-MOD, whereas the highest value is 99% and it is achieved with DDFS of NL-MOD.
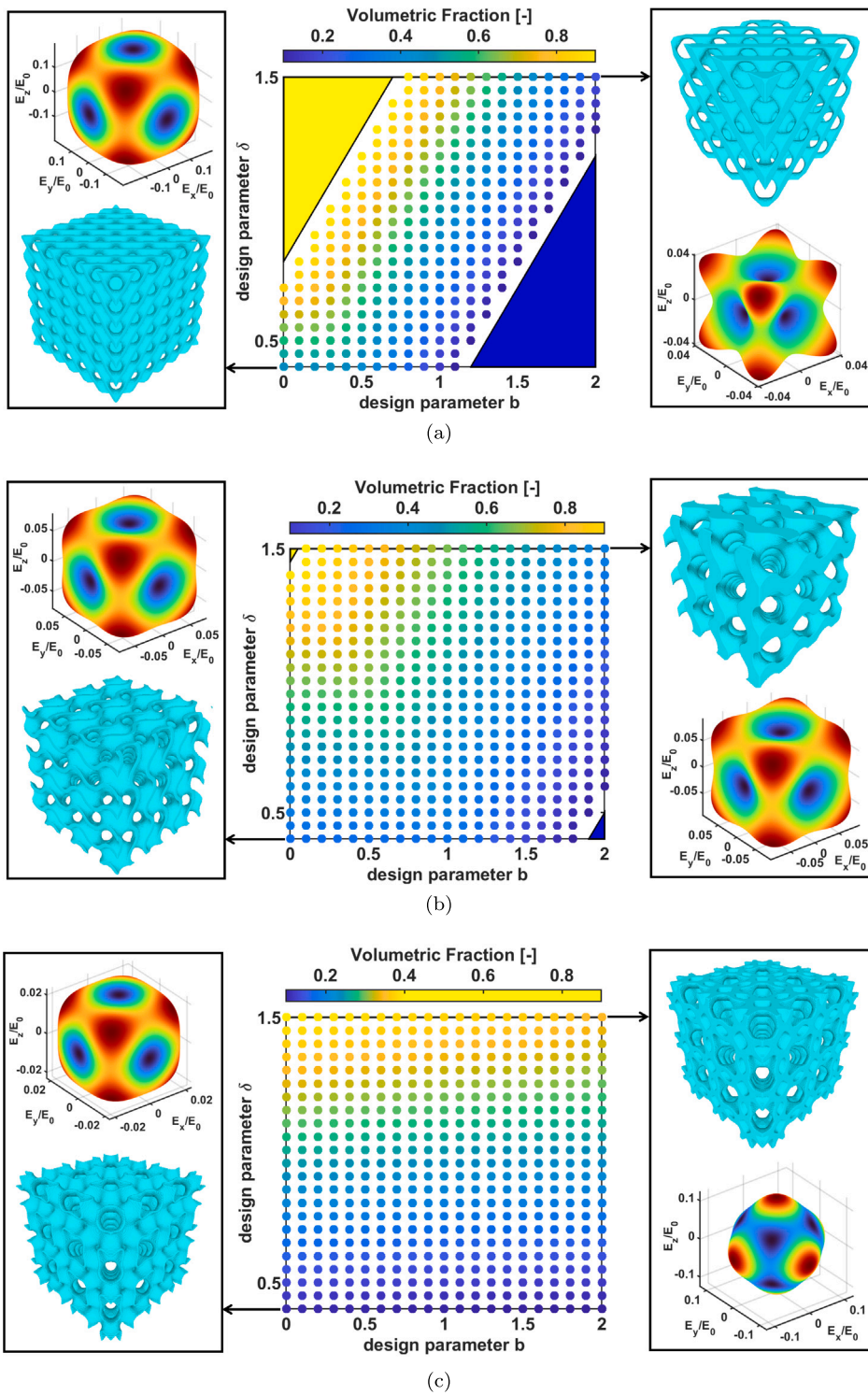
Fig. 4. Representation of the volumetric fraction with respect to the design parameters b and δ in the whole design space of (a) Diamond, (b) Gyroid and (c) IWP. Left and right panels represent the scaffold at its corner and the representation of its stiffness in the space.
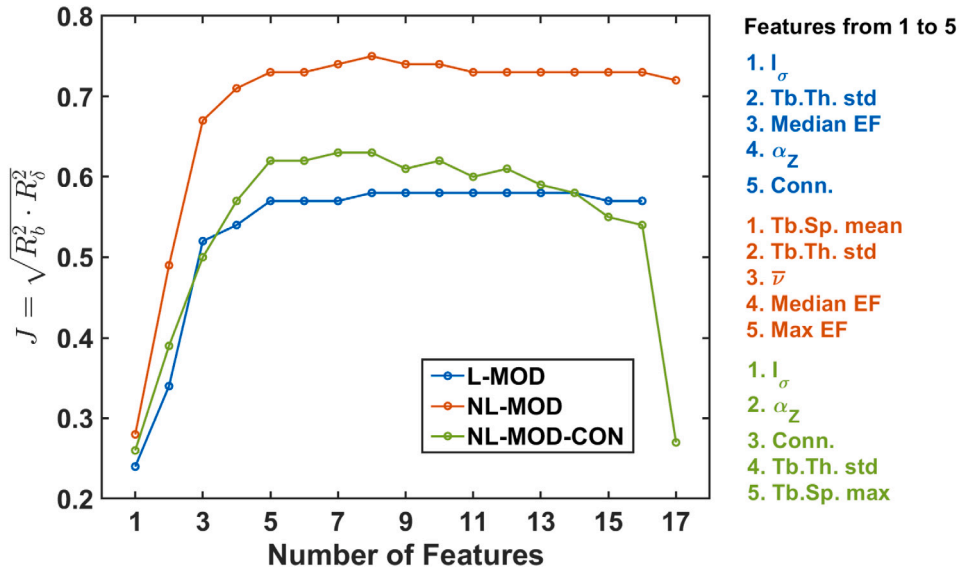
Fig. 5. Value of the J metric on the validation set for each selected feature and the three models. On the right, the first 5 features of each model have been reported.

3.3. Additional assessment of performance

Since the performance of NL-MOD on the test set has achieved better performance than NL-MOD-CON (Table 2), the additional assessment was carried out only for L-MOD and NL-MOD.

The performances of the multinomial logistic regression model have been initially evaluated by considering the number of properly identified geometries. For the non-linear model with DDFS scheme, all geometries have been correctly identified while for the linear model with DDFS scheme 44 out of 50 geometries have been precisely classified. In both models incorporating DKFS scheme, 49 geometries have been accurately identified. In the case of MFS scheme, the linear model has correctly classified 49 out of 50 geometries, whereas the non-linear model has correctly classified 48 geometry types. All the models correctly classify the IWP geometry, whereas the misclassification was between the two remaining geometries.

The spider plots in Fig. 6 represent the median, the 25th percentile and the 75th percentile of the percentage error for each feature used to predict the parameters b and δ across the 50 scaffolds selected from the test set. Generally, for all three feature selection strategies, the non-linear model exhibits better performances than the linear model in terms of median percentage error and interquartile range. The model that achieved the lowest median percentage errors and variability across features was NL-MOD with MFS scheme. In addition, none of these errors were found statistically significantly different than zero, suggesting the presence of a bias between the tested quantities.

Except for the NL-MOD with DDFS scheme, all other approaches result in the exclusion of scaffolds that featured completely void or solid slices, as well as those pinching off of the surface. More specifically, for the linear model with DDFS scheme, two scaffolds are discarded. Similarly, for both the linear and non-linear models with DKFS scheme, one scaffold is discarded. Regarding the linear and non-linear models with MFS scheme, two and three scaffolds are respectively omitted from the analysis.

3.4. Design of a hydroxyapatite scaffold with given mechanical and morphological properties

The TPMS scaffold displaying the closest features has been found by the NL-MOD with MFS scheme using the input feature vector provided in Eq. (12). The model predicted a Gyroid structure with $b = 0.94$ and $\delta = 0.40$. The TPMS scaffold's macroscopic stiffness, as determined by the FE method, is 7.06 GPa, as opposed to the hydroxyapatite scaffold's 7.19 GPa; the TPMS scaffold's strength index is $I_\sigma = 1.48$ MPa, whereas the input value was 0.89 MPa. The TPMS scaffold's wall thickness is 215 μm, marginally less than the input value of 315 μm, but still within the capabilities of Vat Photopolymerization, which can reliably print struts as small as 100 μm. The TPMS wall spacing has been observed to be 876 μm, while the hydroxyapatite scaffold's trabecular spacing measured 798 μm. The trabecular structure was characterized by $\alpha_Z = 1.19$, whereas the Zener index found in the TPMS scaffold is $\alpha_Z = 1.45$.

4. Discussion

This study presents a ML method for figuring out the microstructural configuration of a scaffold for BTE with prescribed features. The ML models were trained using synthetic data produced by the forward model, which is a model with a predetermined
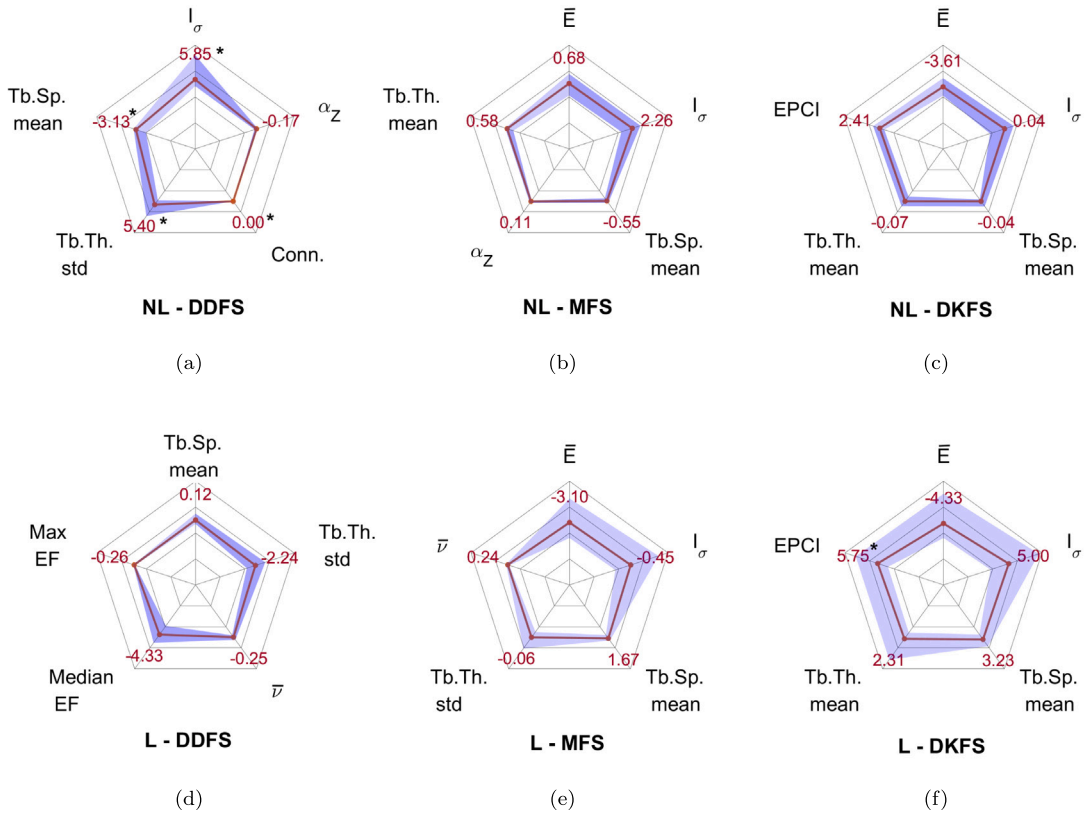
Fig. 6. Median, 25th and 75th percentiles of the percentage errors (%) for each model and feature selection approach. Each axis spans from −50% to +50%. NL and L stand for non-linear and linear, respectively. The ∗ symbol stands for $p < 0.05$.

microstructural layout that can evaluate specific mechanical and physical characteristics of the scaffolds. A restricted class of microstructural configurations has been used, confining our study to three different TPMS geometries. More in details, as for the forward problem, *in silico* experiments have been carried out to characterize the morphometric, permeability and mechanical properties of the scaffolds. The objective of this experiment was to create a dataset suitable for the ML problem. In this work, three ML models and three feature selection schemes have been implemented to determine the input parameters for the design of a scaffold, creating 9 different tools. The implementation of the GFFS algorithm has allowed the selection of features for the estimation of the two design parameters (b and δ), which uniquely identify the architecture of a scaffold for each geometry t. The optimal number of features has been selected to 5 given the negligible improvements on J (Fig. 5) for a higher number of features. Moreover, it represents a reasonable trade-off between performance and complexity, since additional features could not be readily known or accessible during the design phase, as they hold a clear physical and mechanical meaning. Furthermore, Fig. 5 shows that J exhibits higher values for the non-linear model. This can be attributed to the inherent complexity of the model itself and not to the number of model parameters. Indeed, the non-linear model requires $1+4P$ coefficients while the linear model only $1+P$ parameters. However, even equipping the linear model with $\approx 4\times$ the number of the features, the J metric does not reach the same performance achieved by the non-linear model, as shown in Fig. 5. We can then conclude that the improvement was mostly associated to the non-linear component (i.e. the hyperbolic tangent) included in the model, rather than the number of parameters.

The NL-MOD has offered an advantage in terms of flexibility, leading to an improvement in the fitting of data with respect to both L-MOD and NL-MOD-CON. This improvement is due to the non-linear component introduced, which may create non-monotonic relationships between the input feature and output b and δ. For example, the index of strength in NL-MOD with MFS has been found to exhibit a non-monotonic relationship with parameters b (quantified thanks to the additive property of the model), explaining the superior performance in this case. Regarding NL-MOD-CON, the introduction of constraints has caused the non-linear model to behave similar to L-MOD. Since the optimization problems for NL-MOD and NL-MOD-CON set up are non-convex with respect to their parameters, they suffer from (i) sensitivity to initial conditions; and (ii) potential stop in local optima. This could explain why NL-MOD-CON has performed worse than L-MOD even with the same set of input features (DKFS column in Table 2).

The additional analysis on the 50 scaffolds has demonstrated that NL-MOD generally outperforms L-MOD across different feature selection schemes (Fig. 6). However, NL-MOD with DDFS scheme has appeared to be better when compared to the other models on the test set (Table 2), but the median percentage error has been found statistically significantly different from 0 for 4 out of 5
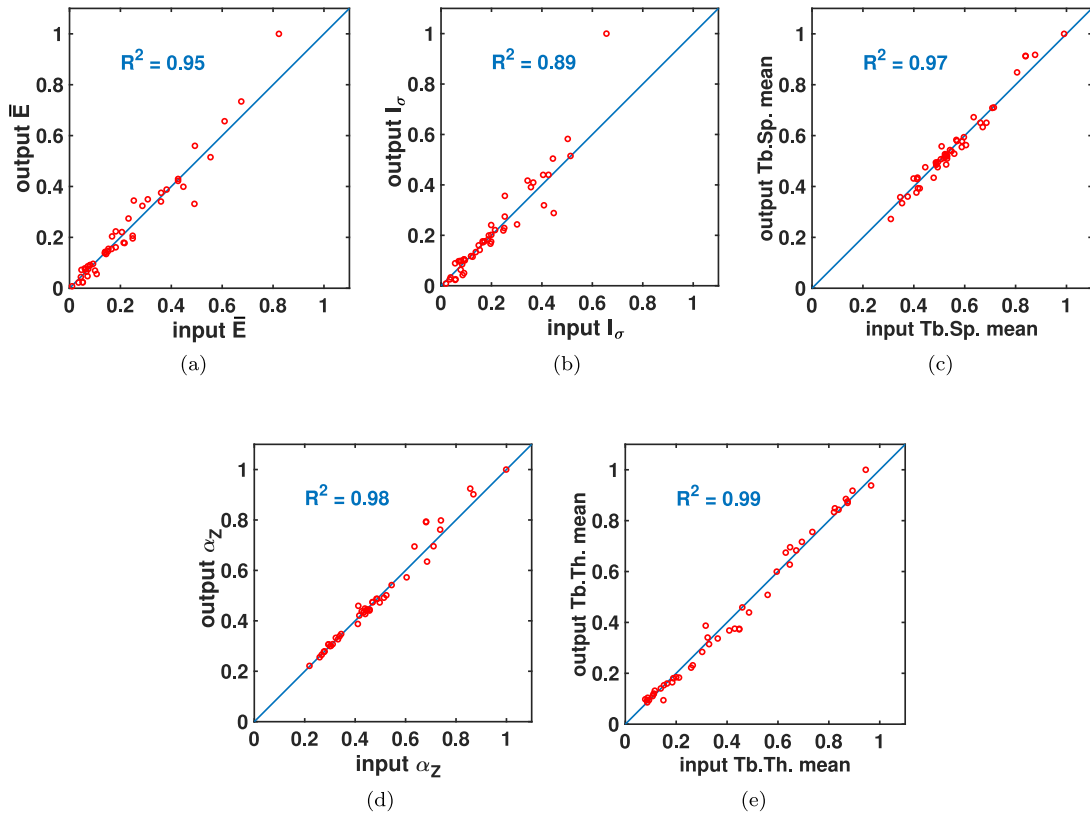
Fig. 7. Correlation coefficient between the features used to feed the NL-MOD with MFS to generate the scaffolds (input) and the features calculated on the generated scaffolds (output) for 50 scaffolds of the test set. All the values have been normalized. (a) Macroscopic stiffness ($\bar{E}$), (b) Index of strength (I_σ), (c) mean pore spacing (Tb.Sp. mean), (d) Zener coefficient (α_Z) and (e) mean wall thickness (Tb.Th. mean).

features (Fig. 6). This could be due to overfitting on the dataset, introduced by the GFFS algorithm which maximizes the J metric without considering a possible bias between the tested quantities.

As a representative example, the performances of the NL-MOD with MFS on the test set have been reported in Fig. 7. This model exhibits a small error and all five features are useful and available in the design phase.

In particular, the stiffness and the index of strength are relevant for the mechanical stability [8,43], the pore spacing is related to the bone growth [44,45], the wall thickness is related to the printability [36,46] and the Zener coefficient used to control the mechanical anisotropy [29]. In Fig. 8 the three geometries are reported to show the differences between the scaffolds designed through ML by using the NL-MOD with MFS and the ones designed during the direct problem. For this example, for each typology of scaffold we selected the one exhibiting a volumetric fraction between 34% and 36%, namely in the range of volumetric fraction typically used in BTE applications [47].

A hydroxyapatite TPMS scaffold that can be produced using Vat Photopolymerization printing technology has been designed using the NL-MOD with MFS. The target features have been selected by considering a trabecular-like scaffold previously analyzed by some of the Authors in [40]. The characteristics of the triply-periodic scaffold that the ML algorithm identified are in close proximity to the majority of the target values. Specifically, it was found that the wall/trabecular spacing and macroscopic stiffness are both within a 10% range. The trabecular thickness is within the technological bounds of Vat Photopolymerization, despite being about 30% less than the target value. The mismatch in the Zener ratio α_Z is 20% higher than the target value. The strength index (I_σ), revealed the largest discrepancy between the target value and the TPMS property; it is 60% higher for the TPMS than for the trabecular-like structure. While the mismatch is on the safe side, the strength index is noticeably off from the target value. Although the TPMS scaffold exhibits a thinner wall thickness and similar solid fraction if compared to the trabecular scaffold, finite element simulations of a uniaxial compression test run on the hydroxyapatite trabecular scaffold and on the TPMS scaffold have revealed that the macroscopic compressive strength for the TPMS scaffold is 7.5 MPa, while the strength for the trabecular structure is 3.34 MPa [40]. There are multiple explanation to this finding. The wall thickness in the TPMS structure is more uniformly distributed throughout the scaffold (with a standard deviation which is 10% of the average thickness) if compared to the trabecular scaffold which, instead, exhibits a standard deviation which is 30% of the average thickness. This implies that the trabecular scaffold has many weak points (thinner structures) where the fracture is attracted, eventually anticipating the overall failure. Furthermore, additional morphological characteristics may be important in determining the mechanical strength of TPMS scaffolds and that
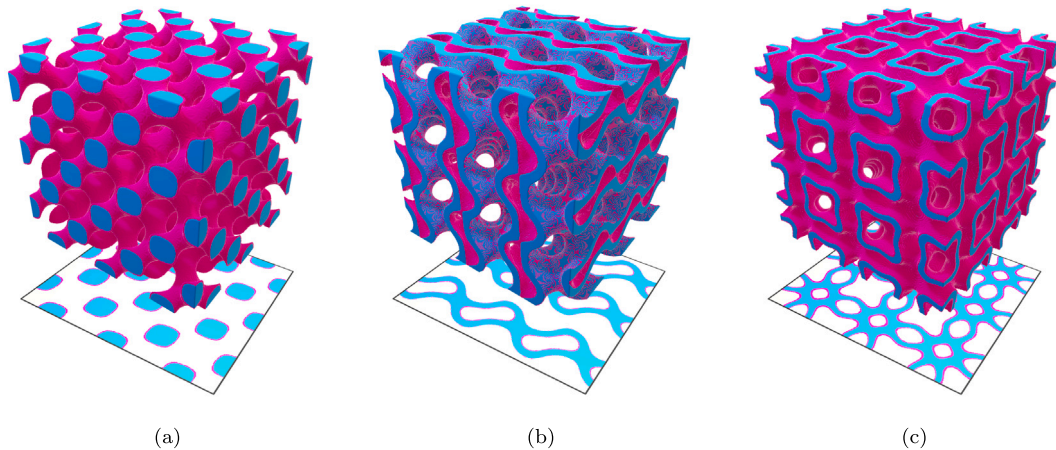
Fig. 8. (a) Diamond, (b) Gyroid, and (c) IWP scaffolds. The blue part represents the common volumetric fraction between the scaffolds obtained during the direct problem, and the scaffolds produced through ML. The purple part represents the under/over amount of volumetric fraction due to the ML error, being 5%, 3% and 4% for Diamond, Gyroid and IWP, respectively. (For interpretation of the references to color in this figure legend, the reader is referred to the web version of this article.)

volumetric percentage and wall thickness may not be the only factors. The TPMS scaffold, in particular, has more connectivity (and connectivity density), which may have contributed to the higher strength. As shown in Fig. 9, in the trabecular-like scaffolds, fractures propagate through the entire thickness of the trabeculae near the interconnections. On the other hand, in TPMS scaffolds, fractures do not traverse the entire cross-section and are distributed in different locations. This should be attributed to the different connectivity. The pattern of fractures in TPMS is not ordered because some cracks may propagate while others do not, as stress concentrates at the tip of the growing fractures, promoting their further growth and resulting in a non-regular pattern. The NL-MOD with MFS scheme did not select the connectivity as a relevant parameter, but it was selected by the NL-MOD with DDFS scheme. This suggests that the connectivity is involved in the mechanical performances of scaffolds and further investigations on its role are needed.

In general, target features may impose competing objectives [48], and the machine learning algorithm aims to achieve a configuration that involves trade-offs, so this should be taken into account when evaluating the mismatch between the target features and the TPMS scaffold features identified by the ML algorithm.

Although AI is nowadays broadly used for the prediction of material properties, at the best of our knowledge, only three studies [26–28] use ML for the prediction of the design parameters starting from the desired scaffold's properties. Kumar et al. [26] proposed an artificial neural network trained to estimate the porosity, the number of pores and their shapes using, as design parameters, the effective thermal conductivity and permeability. Their model was calibrated using about 200 scaffolds with three different shapes of pores placed within each 3D structure. Zheng et al. [27] trained a 3D conditional generative adversarial network able to generate Voronoi-like structures using elastic modulus and volumetric fraction as design parameters. The model was trained using 10 000 scaffolds randomly created, which were then used to calibrate a deep learning model able to generate an endless number of scaffolds with a single pair of design parameters. Liu et al. [28] proposed a neural network to tackle the forward problem (predicting the stiffness coefficients from geometry's parameters) and a regenerative genetic algorithm for the inverse design of a scaffold (finding geometry's parameters from the target stiffness coefficients). For the scope, they generated a dataset consisting of 8000 scaffolds with four TPMS geometries (Primitive, Diamond, Gyroid and Octo) with porosities ranging from 50% to 75%. The scaffolds went through FE simulations for computing the stiffness matrix. The dataset was then used to train the neural network. The main difference between the three aforementioned models and ours was that Kumar et al. [26] and Zheng et al. [27] used only two features, and Liu et al. [28] three features, to predict the design parameters, while we showed that the TPMS geometries were better characterized using five features. It is worth mentioning that in our work, scaffolds have been characterized by properties from different domains, tackling the task in a multidisciplinary way, thereby a higher number of features is required for its design. Here, we considered mechanical, morphometric and physical domains altogether. Therefore, five features can be intended a reasonable quantity for such a complex task.

Solely regarding Zheng et al.'s work [27], they investigated volumetric fractions up to 0.5. As they observed in their study, when inputting the network with design parameters outside the ranges available in the training set, the generated scaffolds displayed incorrect geometries. In our case, for the Diamond and Gyroid geometries, and partly for the IWP as well, we considered the whole range of feasible scaffolds. Despite this should make our models robust to large ranges of design parameters, in general, we do not expect our ML models to provide meaningful results in case the input features are out of the data space. However, identifying such cases is challenging. Techniques from the field of Bayesian methods provide confidence levels for the ML predictions. Such levels can help discarding inputs which were not present in the training set because the confidence would drop significantly. We leave
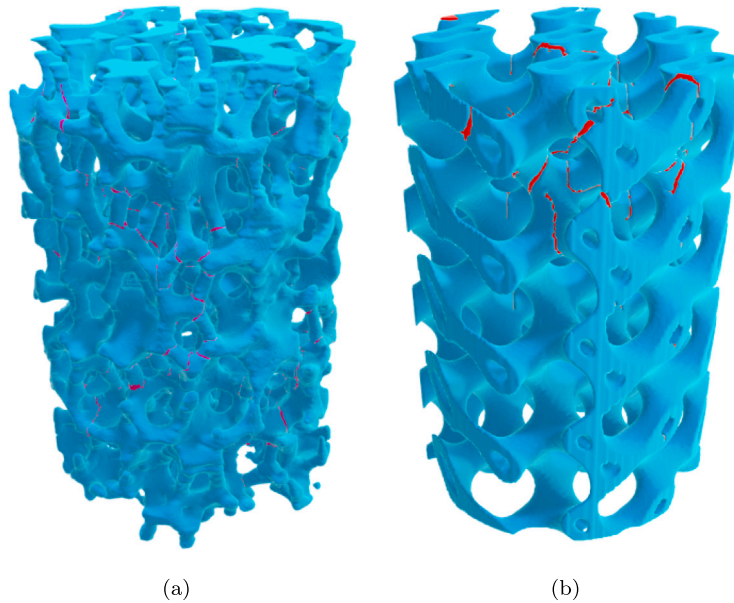
(a)   (b)

Fig. 9. Finite element analysis of uniaxial compressive test: (a) trabecular-like scaffold exhibiting the crack pattern in purple; (b) TPMS gyroid scaffold exhibiting the crack pattern in red. (For interpretation of the references to color in this figure legend, the reader is referred to the web version of this article.)

this investigation to future studies. Finally, differently from Zheng et al.'s approach, our models cannot generate multiple scaffolds with the same design parameters.

In order to limit the computational time, a series of simplifications have been introduced in this study to create the dataset. Firstly, three repetitive units per edge were considered. This decision results in a slight underestimation of the macroscopic stiffness ($\bar{E}$) by approximately 4% [49]. Secondly, the strength index (I_σ) has been computed using a probabilistic model [37] and employed as a substitute for compression strength since fracture simulations are highly time-consuming and cannot be performed on such a number of scaffolds. Fracture simulations using a voxel-wise mesh can be conducted, modeling the crack nucleation and propagation to establish a correlation between I_σ and the simulated strength [50]. Thirdly, for permeability analyses a simplified permeability index was computed, namely EPCI. It has to be considered as a performance index, thereby it is necessary to conduct Computational Fluid Dynamics (CFD) simulations [51,52] to obtain a correlation between the EPCI and the permeability.

Furthermore, the dataset consists of synthetic data rather than real-world data. The printing process and its resulting manufacturing defects on the scaffolds were not taken into account. Geometrical distortion and micro-porosity are the elements that significantly alter designed scaffolds from printed scaffolds [36,50]. As a result, the data distribution may not accurately represent the reality. To ensure the practical applicability of ML models, it is crucial to complement synthetic data with real-world data during model development and validation. This could lead to a more robust ML model and it is left for future investigations.

5. Conclusions

The aim of this paper was to create a new numerical tool for the automatic identification of the microstructure of TPMS scaffolds which simultaneously satisfies multidisciplinary requirements. In particular, mechanical properties like stiffness and strength, mechano-biology parameters like pore size and technological constraints like wall thickness are accounted for. To this purpose linear and non-linear ML models are considered with specific reference to the hydroxyapatite material. The achieved results have shown that the latter offers a better prediction of design parameters with the warning that input parameters may have conflicting objectives, the ML models can successfully design a TPMS scaffold with features prescribed based on biomechanical, mechanobiological and technological constraints. This study represents a significant step forward in the quest for improved bone regeneration therapies which, however, needs to be further developed. Most notably, a critical component that must be considered in the design of efficient BTE scaffolds is the ability of the currently available AM processes to build ceramic devices with high fidelity.

CRediT authorship contribution statement

Silvia Ibrahimi: Writing – review & editing, Writing – original draft, Methodology, Investigation, Data curation. **Luca D'Andrea:** Writing – review & editing, Writing – original draft, Methodology, Investigation. **Dario Gastaldi:** Writing – review & editing, Conceptualization. **Massimo W. Rivolta:** Writing – review & editing, Writing – original draft, Methodology, Investigation, Conceptualization. **Pasquale Vena:** Writing – review & editing, Writing – original draft, Supervision, Methodology, Conceptualization.

Declaration of competing interest

Data availability

No data was used for the research described in the article.

Acknowledgments

Appendix A. Supplementary data

Supplementary material related to this article can be found online at https://doi.org/10.1016/j.cma.2024.116842.

References

[1] Y.-Z. Huang, H.-Q. Xie, X. Li, Scaffolds in bone tissue engineering: Research progress and current applications, in: M. Zaidi (Ed.), Encyclopedia of Bone Biology, Academic Press, Oxford, 2020, pp. 204–215, http://dx.doi.org/10.1016/B978-0-12-801238-3.11205-X, URL https://www.sciencedirect.com/science/article/pii/B978012801238311205X.

[2] H. Bezstarosti, W.J. Metsemakers, E.M. van Lieshout, L.W. Voskamp, K. Kortram, M.A. McNally, L.C. Marais, M.H. Verhofstad, Management of critical-sized bone defects in the treatment of fracture-related infection: A systematic review and pooled analysis, Arch. Orthop. Trauma Surg. 141 (2021) 1215–1230, http://dx.doi.org/10.1007/s00402-020-03525-0.

[3] G.F. de Grado, L. Keller, Y. Idoux-Gillet, Q. Wagner, A.M. Musset, N. Benkirane-Jessel, F. Bornert, D. Offner, Bone substitutes: A review of their characteristics, clinical use, and perspectives for large bone defects management, J. Tissue Eng. 9 (2018) http://dx.doi.org/10.1177/2041731418776819.

[4] T. Tariverdian, F. Sefat, M. Gelinsky, M. Mozafari, Scaffold for bone tissue engineering, in: Handbook of Tissue Engineering Scaffolds: Volume One, Elsevier, 2019, pp. 189–209, http://dx.doi.org/10.1016/b978-0-08-102563-5.00010-1.

[5] M. Shen, Y. Li, F. Lu, Y. Gou, C. Zhong, S. He, C. Zhao, G. Yang, L. Zhang, X. Yang, Z. Gou, S. Xu, Bioceramic scaffolds with triply periodic minimal surface architectures guide early-stage bone regeneration, Bioactive Mater. 25 (2023) 374–386, http://dx.doi.org/10.1016/j.bioactmat.2023.02.012.

[6] P. Yang, J. Xing, J. Liu, F. Luo, X. Wu, B. Yu, M. Deng, J. Xu, T. Hou, Individual tissue-engineered bone in repairing bone defects: A 10-year follow-up study, Tissue Eng. Part A 26 (15–16) (2020) 896–904, http://dx.doi.org/10.1089/ten.tea.2019.0287, PMID: 32027222.

[7] A. Bandyopadhyay, S. Ghosh, A.R. Boccaccini, S. Bose, 3D printing of biomedical materials and devices, J. Mater. Res. 36 (2021) 3713–3724, http://dx.doi.org/10.1557/s43578-021-00407-y.

[8] Q. Fu, E. Saiz, M. Rahaman, A. Tomsia, Bioactive glass scaffolds for bone tissue engineering: State of the art and future perspectives, Mater. Sci. Eng. C 31 (7) (2011) 1245–1256, http://dx.doi.org/10.1016/j.msec.2011.04.022, cited By 371.

[9] Q. Zhang, L. Ma, X. Ji, Y. He, Y. Cui, X. Liu, C. Xuan, Z. Wang, W. Yang, M. Chai, X. Shi, High-strength hydroxyapatite scaffolds with minimal surface macrostructures for load-bearing bone regeneration, Adv. Funct. Mater. 32 (2022) http://dx.doi.org/10.1002/adfm.202204182.

[10] S.V. Bael, Y.C. Chai, S. Truscello, M. Moesen, G. Kerckhofs, H.V. Oosterwyck, J.-P. Kruth, J. Schrooten, The effect of pore geometry on the in vitro biological behavior of human periosteum-derived cells seeded on selective laser-melted Ti6Al4V bone scaffolds, Acta Biomater. 8 (2012) 2824–2834, http://dx.doi.org/10.1016/j.actbio.2012.04.001.

[11] E. Baas, J.H. Kuiper, Y. Yang, M.A. Wood, A.J. El Haj, In vitro bone growth responds to local mechanical strain in three-dimensional polymer scaffolds, J. Biomech. 43 (4) (2010) 733–739, http://dx.doi.org/10.1016/j.jbiomech.2009.10.016, URL https://www.sciencedirect.com/science/article/pii/S0021929009005909.

[12] C. Metz, G.N. Duda, S. Checa, Towards multi-dynamic mechano-biological optimization of 3D-printed scaffolds to foster bone regeneration, Acta Biomater. 101 (2020) 117–127, http://dx.doi.org/10.1016/j.actbio.2019.10.029.

[13] L. Gibson, M. Ashby, Cellular Solids: Structure and Properties, second ed., 2014, pp. 1–510, http://dx.doi.org/10.1017/CBO9781139878326, cited By 275.

[14] L.J. Gibson, Biomechanics of cellular solids, J. Biomech. 38 (3) (2005) 377–399.

[15] D. Yoo, Heterogeneous minimal surface porous scaffold design using the distance field and radial basis functions, Med. Eng. Phys. 34 (5) (2012) 625–639, http://dx.doi.org/10.1016/j.medengphy.2012.03.009, URL https://www.sciencedirect.com/science/article/pii/S1350453312000574.

[16] D.-J. Yoo, Advanced porous scaffold design using multi-void triply periodic minimal surface models with high surface area to volume ratios, Int. J. Precis. Eng. Manuf. 15 (8) (2014) 1657–1666, http://dx.doi.org/10.1007/s12541-014-0516-5.

[17] X. Zheng, Z. Fu, K. Du, C. Wang, Y. Yi, Minimal surface designs for porous materials: from microstructures to mechanical properties, J. Mater. Sci. 53 (14) (2018) 10194–10208, http://dx.doi.org/10.1007/s10853-018-2285-5.

[18] P.G. Coelho, S.J. Hollister, C.L. Flanagan, P.R. Fernandes, Bioresorbable scaffolds for bone tissue engineering: Optimal design, fabrication, mechanical testing and scale-size effects analysis, Med. Eng. Phys. 37 (3) (2015) 287–296, http://dx.doi.org/10.1016/j.medengphy.2015.01.004, Additive Manufacturing;Biofabrication;Bioresorbable scaffolds;Bone scaffolds;Bone tissue engineering;Computational assumptions;Homogenization approach;Multiscale models;.

[19] E. Davoodi, H. Montazerian, A.S. Mirhakimi, M. Zhianmanesh, O. Ibhadode, S.I. Shahabad, R. Esmaeilizadeh, E. Sarikhani, S. Toorandaz, S.A. Sarabi, R. Nasiri, Y. Zhu, J. Kadkhodapour, B. Li, A. Khademhosseini, E. Toyserkani, Additively manufactured metallic biomaterials, Bioactive Mater. 15 (2022) 214–249, http://dx.doi.org/10.1016/j.bioactmat.2021.12.027, URL https://www.sciencedirect.com/science/article/pii/S2452199X21006010.

[20] M. Naveen Kumar, B. Gurumoorthy, Design of porous structures, Comput.-Aided Des. Appl. 18 (4) (2020) 704–713, http://dx.doi.org/10.14733/cadaps.2021.704-713, Cited by: 0; All Open Access, Bronze Open Access.

[21] O. Ronneberger, P. Fischer, T. Brox, U-Net: Convolutional networks for biomedical image segmentation, in: N. Navab, J. Hornegger, W.M. Wells, A.F. Frangi (Eds.), Medical Image Computing and Computer-Assisted Intervention, MICCAI 2015, Springer International Publishing, Cham, 2015, pp. 234–241.

[22] A. de Medeiros Brito Junior, A.D. DÓria Neto, J. Dantas de Melo, L.M. Garcia Goncalves, An adaptive learning approach for 3-D surface reconstruction from point clouds, IEEE Trans. Neural Netw. 19 (6) (2008) 1130–1140, http://dx.doi.org/10.1109/TNN.2008.2000390.

[23] J. Kim, J.A. McKee, J.J. Fontenot, J.P. Jung, Engineering tissue fabrication with machine intelligence: Generating a blueprint for regeneration, Front. Bioeng. Biotechnol. 7 (2020) http://dx.doi.org/10.3389/fbioe.2019.00443, URL https://www.frontiersin.org/article/10.3389/fbioe.2019.00443.

[24] M.D.B. Barrera, F. Franco-Martínez, A.D. Lantada, Artificial intelligence aided design of tissue engineering scaffolds employing virtual tomography and 3D convolutional neural networks, Materials 14 (18) (2021) 5278, http://dx.doi.org/10.3390/ma14185278.

[25] S. Ma, Q. Tang, Y. Liu, Q. Feng, Prediction of mechanical properties of three-dimensional printed lattice structures through machine learning, J. Comput. Inf. Sci. Eng. 22 (2022) 031008, http://dx.doi.org/10.1115/1.4053077.

[26] M. Kumar, B. Gurumoorthy, Design of porous structures, J. Mater. Sci. 18 (4) (2018) 704–713, http://dx.doi.org/10.14733/cadaps.2021.704-713.

[27] X. Zheng, T.-T. Chen, X. Jiang, M. Naito, I. Watanabe, Deep-learning-based inverse design of three-dimensional architected cellular materials with the target porosity and stiffness using voxelized voronoi lattices, Sci. Technol. Adv. Mater. 24 (1) (2023) http://dx.doi.org/10.1080/14686996.2022.2157682.

[28] W. Liu, Y. Zhang, Y. Lyu, S. Bosiakov, Y. Liu, Inverse design of anisotropic bone scaffold based on machine learning and regenerative genetic algorithm, Front. Bioeng. Biotechnol. 11 (2023) http://dx.doi.org/10.3389/fbioe.2023.1241151, URL https://www.frontiersin.org/articles/10.3389/fbioe.2023.1241151/full.

[29] J. Feng, B. Liu, Z. Lin, J. Fu, Isotropic porous structure design methods based on triply periodic minimal surfaces, Mater. Des. 210 (2021) http://dx.doi.org/10.1016/j.matdes.2021.110050.

[30] C. Soyarslan, V. Blümer, S. Bargmann, Tunable auxeticity and elastomechanical symmetry in a class of very low density core-shell cubic crystals, Acta Mater. 177 (2019) 280–292, http://dx.doi.org/10.1016/j.actamat.2019.07.015.

[31] R. Domander, A. Felder, M. Doube, BoneJ2 - refactoring established research software [version 2; peer review: 3 approved], Wellcome Open Res. 6 (37) (2021) http://dx.doi.org/10.12688/wellcomeopenres.16619.2.

[32] H. Sun, H. Al-Marzouqi, S. Vega, EPCI: A new tool for predicting absolute permeability from computed tomography images, GEOPHYSICS 84 (3) (2019) F97–F102, http://dx.doi.org/10.1190/geo2018-0653.1.

[33] C. Flaig, P. Arbenz, A scalable memory efficient multigrid solver for micro-finite element analyses based on CT images, Parallel Comput. 37 (2011) 846–854, http://dx.doi.org/10.1016/j.parco.2011.08.001.

[34] C.M. Zener, Elasticity and Anelasticity of Metals, University of Chicago Press, Chicago, 1948.

[35] Y. Lu, W. Zhao, Z. Cui, H. Zhu, C. Wu, The anisotropic elastic behavior of the widely-used triply-periodic minimal surface based scaffolds, J. Mech. Behav. Biomed. Mater. 99 (6) (2019) 56–65, http://dx.doi.org/10.1016/j.jmbbm.2019.07.012.

[36] L. D'Andrea, D. Gastaldi, F. Baino, E. Verné, G. Saccomano, L. D'Amico, E. Longo, M. Schwentenwein, P. Vena, Mechanical characterization of miniaturized 3D-printed hydroxyapatite parts obtained through vat photopolymerization: An experimental study, J. Mech. Behav. Biomed. Mater. 141 (2023) 105760, http://dx.doi.org/10.1016/j.jmbbm.2023.105760, URL https://linkinghub.elsevier.com/retrieve/pii/S1751616123001133.

[37] M. Genet, M. Houmard, S. Eslava, E. Saiz, A.P. Tomsia, A two-scale Weibull approach to the failure of porous ceramic structures made by robocasting: Possibilities and limits, J. Eur. Ceramic Soc. 33 (4) (2013) 679–688, http://dx.doi.org/10.1016/j.jeurceramsoc.2012.11.001.

[38] X. Fan, E. Case, I. Gheorghita, M. Baumann, Weibull modulus and fracture strength of highly porous hydroxyapatite, J. Mech. Behav. Biomed. Mater. 20 (2013) 283–295, http://dx.doi.org/10.1016/j.jmbbm.2013.01.031.

[39] T. Cormen, E. Leiserson, R. Rivest, C. Stein, Introduction to Algorithms, third ed., The MIT Press, 2009.

[40] L. D'Andrea, D. Gastaldi, F. Baino, E. Verné, M. Schwentenwein, G. Örlygsson, P. Vena, Computational models for the simulation of the elastic and fracture properties of highly porous 3D -printed hydroxyapatite scaffolds, Int. J. Numer. Methods Biomed. Eng. (2023) http://dx.doi.org/10.1002/cnm.3795, URL https://onlinelibrary.wiley.com/doi/10.1002/cnm.3795.

[41] F. Baino, G. Magnaterra, E. Fiume, A. Schiavi, L.-P. Tofan, M. Schwentenwein, E. Verné, Digital light processing stereolithography of hydroxyapatite scaffolds with bone-like architecture, permeability, and mechanical properties, J. Am. Ceram. Soc. 105 (3) (2022) 1648–1657, http://dx.doi.org/10.1111/jace.17843, arXiv:https://ceramics.onlinelibrary.wiley.com/doi/pdf/10.1111/jace.17843, URL https://ceramics.onlinelibrary.wiley.com/doi/abs/10.1111/jace.17843.

[42] E. Farina, D. Gastaldi, F. Baino, E. Vernè, J. Massera, G. Orlygsson, P. Vena, Micro computed tomography based finite element models for elastic and strength properties of 3D printed glass scaffolds, Acta Mech. Sin. 37 (2) (2021) 292–306, http://dx.doi.org/10.1007/s10409-021-01065-3, URL https://ui.adsabs.harvard.edu/abs/2021AcMSn..37..292F.

[43] Q. Fu, E. Saiz, M.N. Rahaman, A.P. Tomsia, Toward strong and tough glass and ceramic scaffolds for bone repair, Adv. Funct. Mater. 23 (2013) 5461–5476, http://dx.doi.org/10.1002/adfm.201301121.

[44] A. Barba, A. Diez-Escudero, Y. Maazouz, K. Rappe, M. Espanol, E.B. Montufar, M. Bonany, J.M. Sadowska, J. Guillem-Marti, C. Öhman-Mägi, C. Persson, M.C. Manzanares, J. Franch, M.P. Ginebra, Osteoinduction by foamed and 3D-printed calcium phosphate scaffolds: Effect of nanostructure and pore architecture, ACS Appl. Mater. Interfaces 9 (2017) 41722–41736, http://dx.doi.org/10.1021/acsami.7b14175.

[45] A. Barba, Y. Maazouz, A. Diez-Escudero, K. Rappe, M. Espanol, E.B. Montufar, C. Öhman-Mägi, C. Persson, P. Fontecha, M.C. Manzanares, J. Franch, M.P. Ginebra, Osteogenesis by foamed and 3D-printed nanostructured calcium phosphate scaffolds: Effect of pore architecture, Acta Biomater. 79 (2018) 135–147, http://dx.doi.org/10.1016/j.actbio.2018.09.003.

[46] A. Schiavi, E. Fiume, G. Orlygsson, M. Schwentenwein, E. Verné, F. Baino, High-reliability data processing and calculation of microstructural parameters in hydroxyapatite scaffolds produced by vat photopolymerization, J. Eur. Ceramic Soc. (2022).

[47] V. Karageorgiou, D.L. Kaplan, Porosity of 3D biomaterial scaffolds and osteogenesis, Biomaterials 26 27 (2005) 5474–5491.

[48] A. Entezari, N.C. Liu, Z. Zhang, J. Fang, C. Wu, B. Wan, M. Swain, Q. Li, Nondeterministic multiobjective optimization of 3D printed ceramic tissue scaffolds, J. Mech. Behav. Biomed. Mater. 138 (2023) http://dx.doi.org/10.1016/j.jmbbm.2022.105580.

[49] I. Maskery, L. Sturm, A. Aremu, A. Panesar, C. Williams, C. Tuck, R. Wildman, I. Ashcroft, R. Hague, Insights into the mechanical properties of several triply periodic minimal surface lattice structures made by polymer additive manufacturing, Polymer 152 (3) (2018) 62–71, http://dx.doi.org/10.1016/j.polymer.2017.11.049.

[50] L. D'Andrea, D. Gastaldi, E. Verné, F. Baino, J. Massera, G. Örlygsson, P. Vena, Mechanical properties of robocast glass scaffolds assessed through micro-CT-based finite element models, Materials 15 (2022) http://dx.doi.org/10.3390/ma15186344.

[51] T. Pires, J. Santos, R.B. Ruben, B.P. Gouveia, A.P. Castro, P.R. Fernandes, Numerical-experimental analysis of the permeability-porosity relationship in triply periodic minimal surfaces scaffolds, J. Biomech. 117 (2021) http://dx.doi.org/10.1016/j.jbiomech.2021.110263.

[52] R. Asbai-Ghoudan, S.R. de Galarreta, N. Rodriguez-Florez, Analytical model for the prediction of permeability of triply periodic minimal surfaces, J. Mech. Behav. Biomed. Mater. 124 (2021) http://dx.doi.org/10.1016/j.jmbbm.2021.104804.